Earth Syst. Sci. Data, 17, 3189–3202, 2025
https://doi.org/10.5194/essd-17-3189-2025

Open Access Earth System Science Data

A high-resolution temperature–salinity dataset observed by autonomous underwater vehicles for the evolution of mesoscale eddies and associated submesoscale processes in the South China Sea

Chunhua Qiu[1,2], Zhenyang Du[1,2], Haibo Tang[1,2], Zhenhui Yi[1,2], Jiawei Qiao[1,2], Dongxiao Wang[1,2], Xiaoming Zhai[3], and Wenbo Wang[1,2]

[1]School of Marine Sciences, State Key Laboratory of Environmental Adaptability for Industrial Products, Sun Yat-Sen University, and Southern Marine Science and Engineering Guangdong Laboratory (Zhuhai), Zhuhai, China
[2]Guangdong Provincial Key Laboratory of Marine Resources and Coastal Engineering, School of Marine Sciences, Sun Yat-sen University, Guangzhou 510275, China
[3]Centre for Ocean and Atmospheric Sciences, School of Environmental Sciences, University of East Anglia, Norwich, UK

Correspondence: Dongxiao Wang (dxwang@mail.sysu.edu.cn)

Received: 4 August 2024 – Discussion started: 9 September 2024
Revised: 18 March 2025 – Accepted: 11 April 2025 – Published: 3 July 2025

Abstract. Marginal seas are often characterized by dynamic mesoscale eddies (MEs), whose evolution plays a critical role in regulating global oceanic energy budgets, triggering submesoscale processes with strong vertical velocity, and facilitating biogeochemical transport. However, traditional observation methods, constrained by passive sampling modes, struggle to resolve the temporal evolution of MEs and associated submesoscale processes at kilometer-scale resolutions. Autonomous underwater vehicles (AUVs) and underwater gliders (UGs), operating in active sampling modes, provide spatio-temporal synchronized measurements of these highly dynamic features. Here, we present a 9-year (2014–2022) high-resolution temperature–salinity dataset collected by AUVs/UGs in the South China Sea (SCS), accessible via https://doi.org/10.57760/sciencedb.11996 (Qiu et al., 2024b). In total, the dataset comprises 11 cruise experiments that deployed 50 UGs and two AUVs, achieving spatial and temporal resolutions of <7 km and <7 h, respectively. This dataset offers unprecedented insights into ME evolution life stages, covering the zones of an eddy's birth, propagation, and dissipation. A total of 40 % of the data resolve submesoscale processes (<1 km, <4 h), capturing dynamic instabilities along and across frontal zones at eddy peripheries. This dataset has the potential to improve the forecast accuracy in physical and biogeochemistry numerical models. Much more aggressive field investigation programs will be promoted by the National Natural Science Foundation of China in the future.

1 Introduction

The evolution of mesoscale eddies (MEs), characterized by intense geostrophic strain rates, leads to the generation of submesoscale processes with kilometer-scale spatial resolutions (McWilliams, 2016). This dynamic interplay requires observational systems with high spatio-temporal synchronization and enhanced resolution capabilities. MEs obtain kinetic energy from large-scale currents and subsequently dissipate to submesoscale or finer-scale processes in the slope regions via combined shear and baroclinic instabilities (Oey, 1995; Okkonen et al., 2003). Marginal seas (such as the Gulf of Mexico or the Mediterranean Sea) are usually filled with MEs (Rossby number $R_o = U/fL \approx 0.1$), alongside smaller-scale processes ($R_o > 1$). The South China Sea (SCS), as a tropical marginal sea, demonstrates particularly vigorous ME dynamics (Chen et al., 2011; Wang et al., 2003; Xiu et al., 2010). These coherent vortices, spanning 50–300 km horizontally and persisting several weeks to months, play vital roles in the transport of matter and energy (Chelton et al., 2007; Morrow et al., 2004).

Contemporary observation platforms for MEs include shipborne surveys, satellite remote sensing, Argo float arrays, Lagrangian drifters, autonomous underwater vehicles (AUVs), and underwater gliders (UGs). While ship-based observations are the most fundamental to investigate MEs' general structures, their temporal resolution limits continuous evolution tracking. Satellite altimetry provides comprehensive surface signatures of MEs, including spatio-temporal metrics, radius evolution, and trajectory mapping (Chelton et al., 2011). Four primary ME generation hotspots have been identified in the SCS: southwest of Taiwan, northwest of the Luzon Islands, the Xisha Islands region, and the eastern Vietnamese coastal zone (Hwang and Chen, 2000; Wang et al., 2003; Nan et al., 2011). ME propagation patterns (westward, southwestward, or northwestward) are predominantly governed by first-baroclinic Rossby wave dynamics (Lin et al., 2007; Xiu et al., 2010; Chen et al., 2011). Since 2002, a large number of Argo arrays have been deployed, providing routine measurements to describe the vertical structures of MEs (He et al., 2018; Table 1). However, the spatio-temporal resolutions of Argo profiles are approximately 100 km and 10 d, remaining insufficient to capture the high-frequency variability of MEs and submesoscale processes (Table 1).

Attributed to the active tracking, AUVs and UGs have become increasingly more important tools for exploring marine environments over the last 2 decades. They have the advantages of being low cost, long-lasting, controllable, and reusable. Our research consortium has acquired high-resolution spatio-temporal datasets through coordinated UG and AUV deployments across ME features. UGs became available to the marine science community in 2004, and they adjust buoyancy to generate gliding motion through water columns by a pair of wings (Rudnick et al., 2004; Caffaz et al., 2010). These UG platforms execute "sawtooth" transects at sustained velocities of $\sim 0.3\,\mathrm{m\,s^{-1}}$, while AUVs are propeller-driven, acting by combining "sawtooth" and "cruise" modes at a maximum speed of $1\,\mathrm{m\,s^{-1}}$ (Hobson et al., 2012). For a representative SCS ME with a 100 km radius, full feature transection requires approximately 2.7 d for either platform type. Both platforms carry conductivity-temperature-depth (CTD) sensors for concurrent thermohaline structure mapping, enabling successful detection of dynamic features, such as the warming trend in the Gulf Stream (Todd and Ren, 2023) and the water mass exchanges between the Bay of Bengal and the Arabian Sea (Rainville et al., 2022). Our systematic observation program initiated UG deployments in 2014 (Qiu et al., 2015) and commenced AUV field campaigns in 2018 (Huang et al., 2019; Qiu et al., 2020). We present a consolidated 9-year dataset (2014–2022) from SCS operations, demonstrating the unique capabilities of these platforms in resolving ME evolution dynamics and associated submesoscale processes.

2 Datasets

2.1 UG and AUV experiment sites

Our experimental design specifically targeted ME evolution and submesoscale process characterization. This study employs two types of Chinese-developed UG platforms: "Sea-Wing" (Yu et al., 2011) and "Petrel" (Wu et al., 2011). Since 2014, we have conducted 11 field campaigns in the northern SCS, deploying 50 UGs and two AUVs to collect 13 491 temperature–salinity profiles. Platform deployment parameters, including the deploying time, installed sensors, and diving depths of UGs/AUVs for each experiment are shown in Table 2. Complete mission metadata (vehicle serial number, waypoints, matching time, latitude, and longitude) are archived in the data using the *.nc format. The bold terms in Table 2 highlight the UG arrays consisting of ≥ 3 units. Notably, in the experiments of 2017, 2019, and 2020, more than 10 UGs were deployed to resolve the three-dimensional structures of the MEs.

2.2 Intercomparison of UG and AUV resolutions

The trajectories of AUVs and UGs are depicted in Fig. 1. Each trajectory is superimposed on sea level anomaly (SLA) fields. The maximum absolute value of an SLA is the ME center. Note that all the UGs and AUVs crossed MEs. Spatio-temporal sampling characteristics are presented in Fig. 2. The horizontal resolution reveals two distinct regimes: 4–7 km resolution dominated the 2014, 2015, and 2019 campaigns (blue histograms), while sub-3 km sampling was achieved in the other years. The temporal sampling intervals exhibited similar bimodal distribution, reaching an optimal 1–2 h cadence during the 2017, July 2021, and 2022 deployments (Fig. 2c, f, and h), compared to the 4–7 h resolutions in the remaining experiments. This observational matrix demonstrates that 100 % of datasets resolve ME-scale dynamics (50–300 km spectral range), while 40 % of campaigns attained sufficient resolution to capture submesoscale features (<3 km; <4 h characteristic scale) through synergistic UG/AUV coordination.

3 Data quality control method

Prior to investigating the three-dimensional structures of MEs, we performed rigorous data quality control (QC) for the UG and AUV datasets.

Table 1. Previous observational studies of mesoscale eddies (MEs) in the South China Sea.

Platforms	Authors	ME sources
Ship observation (CTD station)	Dale (1956)	Cool pool near Vietnam
	Wang (1987)	Warm eddy southwest of Taiwan Islands
	Xu and Su (1997)	Northwest of Luzon Islands; named Luzon cold eddy
	Li et al. (1998)	Warm eddy northeast of northern SCS
	Chu et al. (1998)	Eddy pair in central part of SCS
	Fang et al. (2002)	Vietnam warm eddy
Satellite observations (sea level anomaly; velocity)	Hwang and Chen (2000); Wang et al. (2003; Nan et al. 2011)	Topex/Poseidon altimeter data, 94 cold eddies, 124 warm eddies. Southwest of Taiwan Islands, northwest of Luzon Islands, east of Vietnam.
	Lin et al. (2007); Chen et al. (2011); Xiu et al. (2010)	Radius, life cycle, tracking, seasonal and interannual variations of mesoscale eddies
	He et al. (2016)	The role of ENSO on interannual variation in Luzon Strait mesoscale eddies
	He et al. (2019)	MEs' influence on chlorophyll *a*
Argo; mooring	Li et al. (2022)	Vertical tilt of mesoscale eddy
	He et al. (2018)	Reconstruction data combining altimeter and Argo observations, revisit the three-dimensional structures of MEs
	Zhang et al. (2017)	By using mooring array, investigate eddy looping from the Luzon Strait

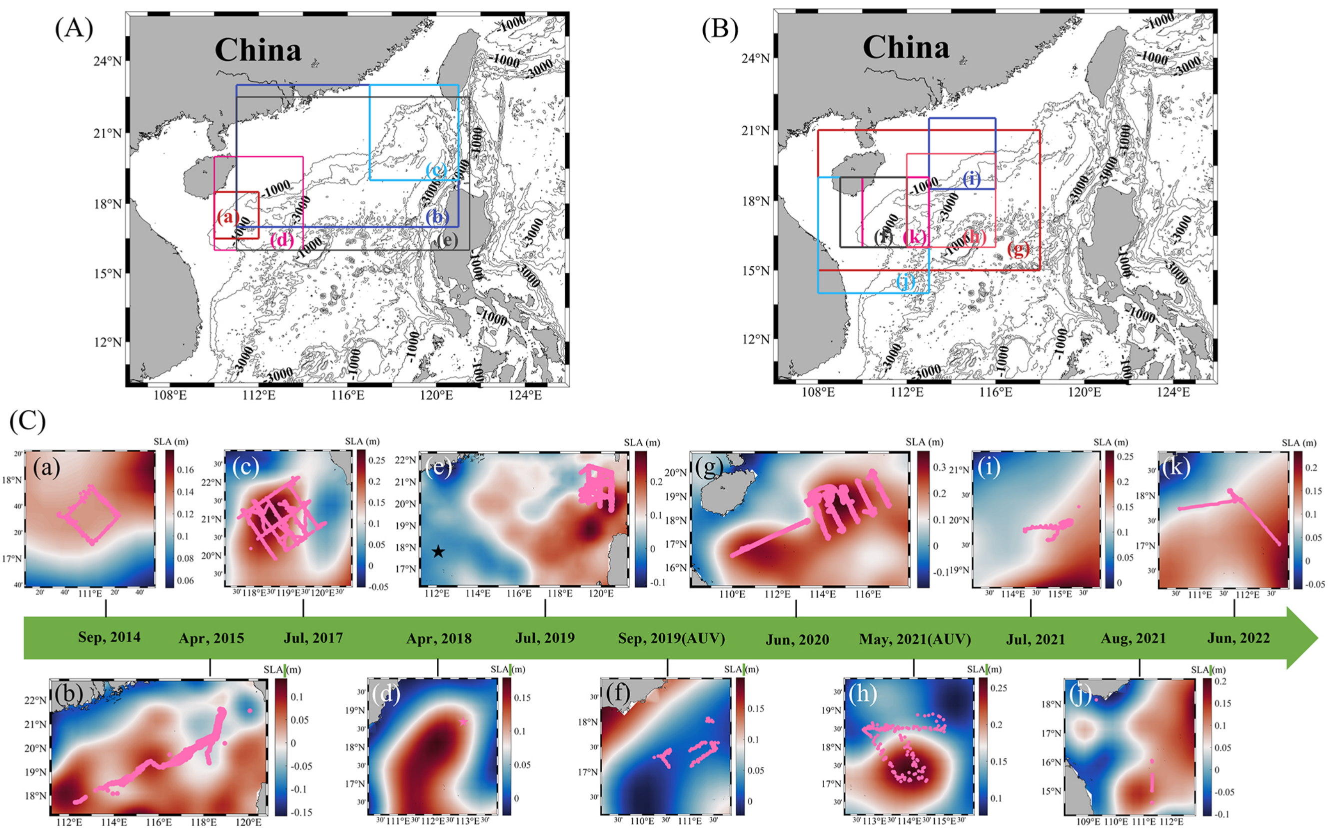

Figure 1. Underwater glider (UG) and autonomous underwater vehicle (AUV) observation sites. **(a)** Observation area for subplots (**c**.a)–(**c**.e); **(b)** area for subplots (**c**.f)–(**c**.j). The gray lines in **(a)** and **(b)** are the water depths. (**c**.a)–(**c**.k) Observation stations (pink dots) with mean sea level anomalies (shading colors). The observation times are (**c**.a) September 2014; (**c**.b) April 2015; (**c**.c) July 2017; (**c**.d) April 2018; (**c**.e) July 2019; (**c**.f) September 2019; (**c**.g) June 2020; (**c**.h) May 2021; (**c**.i) July 2021; (**c**.j) August 2021; and (**c**.k) June 2022.

Table 2. Available datasets from UGs and AUVs. The bold terms highlight the UG arrays consisting of ≥ 3 units.

Number	Equipment	Time	Number of qualified profiles	Number of eliminated profiles (stage)	Number of pieces of equipment	Sensor of equipment (*: with shipped CTD)	Diving depth of equipment	Observing purpose
1	UG	19 Sep–15 Oct 2014; 26 d	227	0	1 UG	Seabird Glider Payload CTD (GPCTD)	1000 m	Mixed layer heat budget; sea trials
2	**UG**	**18 Apr–6 Jul 2015**; **78 d**	**1,358**	**1 (Syntax_Test)**	**3 UGs, Network**	**Seabird GPCTD**	**1000 m**	**Structures of MEs**
3	**UG**	**14 Jul–13 Aug 2017; 30 d**	**2,902**	**99 (Syntax Test)**	**10 UGs, Network**	**Seabird GPCTD**	**300 m (3) 1000 m (7)**	**ME response to TC**
4	UG	22 Apr–23 May 2018; 31 d	239	0	1 UG, Virtual mooring	Seabird GPCTD	1000 m	Structures of MEs
5	UG	13 Jul–30 Sept 2019; 77 d	3,672	0	17 UGs, Network	Seabird GPCTD *	1000 m (17)	Slope intrusion of MEs
6	AUV	18 Sept–23 Oct 2019; 35 d	131	0	1 AUV	SBE37 CTD; DVL^{++}	300 m	Evolution of MEs
7	**UG**	**26 Jun–27 Aug 2020; 60 d**	**3,793**	**7 (Syntax Test)**	**12 UGs**	**Seabird GPCTD**	**1000 m**	**Slope current**
8	UG	26 Jul–8 Aug 2021; 13 d	307	155 (Climatology_Test and Syntax_Test);	2 UGs	RBR legato CTD	300 m (1) 1000 m (1)	Edge of ME
9	UG	7–27 Aug 2021; 20 d	215	0	2 UGs	Seabird GPCTD	1000 m	Edge of ME
10	AUV	9 May–29 Jul 2021; 80 d	168	0	1 AUV	SBE37 CTD	300 m	Evolution of MEs
11	UG	23 Jun–6 Jul 2022; 13 d	217	0	2 UGs	Seabird GPCTD	1000 m	Edge of ME
Total	/	463 d	13,229	262	50 UGs, 2 AUVs	/	/	Structures and evolution of MEs

ME: mesoscale eddy; AUV: autonomous underwater vehicle; UG: underwater glider.

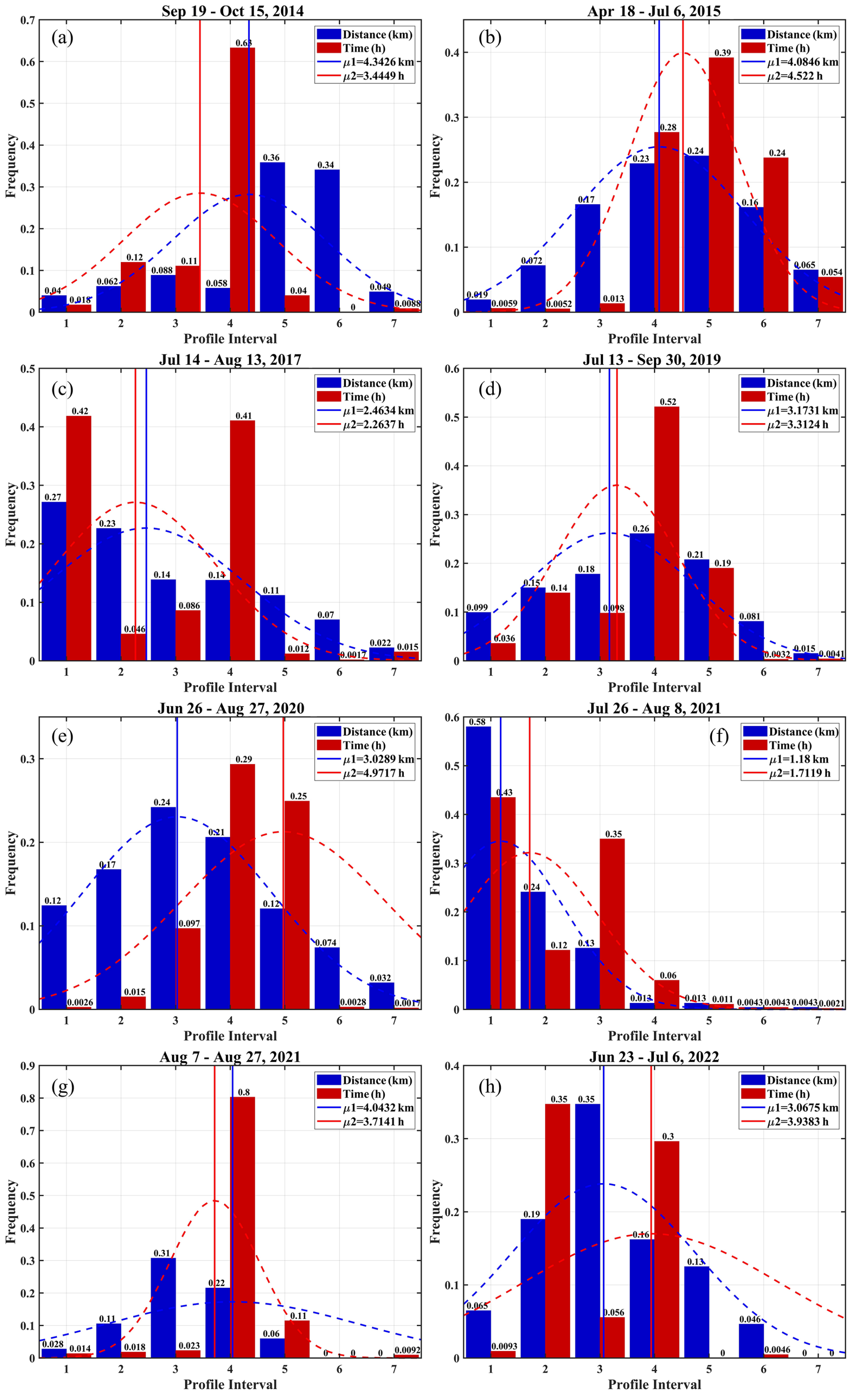

Figure 2. Frequency of spatial (blue bar) and temporal (red bar) sample intervals. "Profile interval" indicates the spatial interval (red) and temporal interval (blue). Bars are the probabilities. Dashed lines are normal distributions of the spatial (red) and temporal (blue) intervals. Mean values of the spatial and temporal intervals are depicted by the red and blue solid lines, respectively. The observation times are **(a)** September 2014; **(b)** April 2015; **(c)** July 2017; **(d)** July 2019; **(e)** June 2020; **(f)** July 2021; **(g)** August 2021; and **(h)** June 2022.

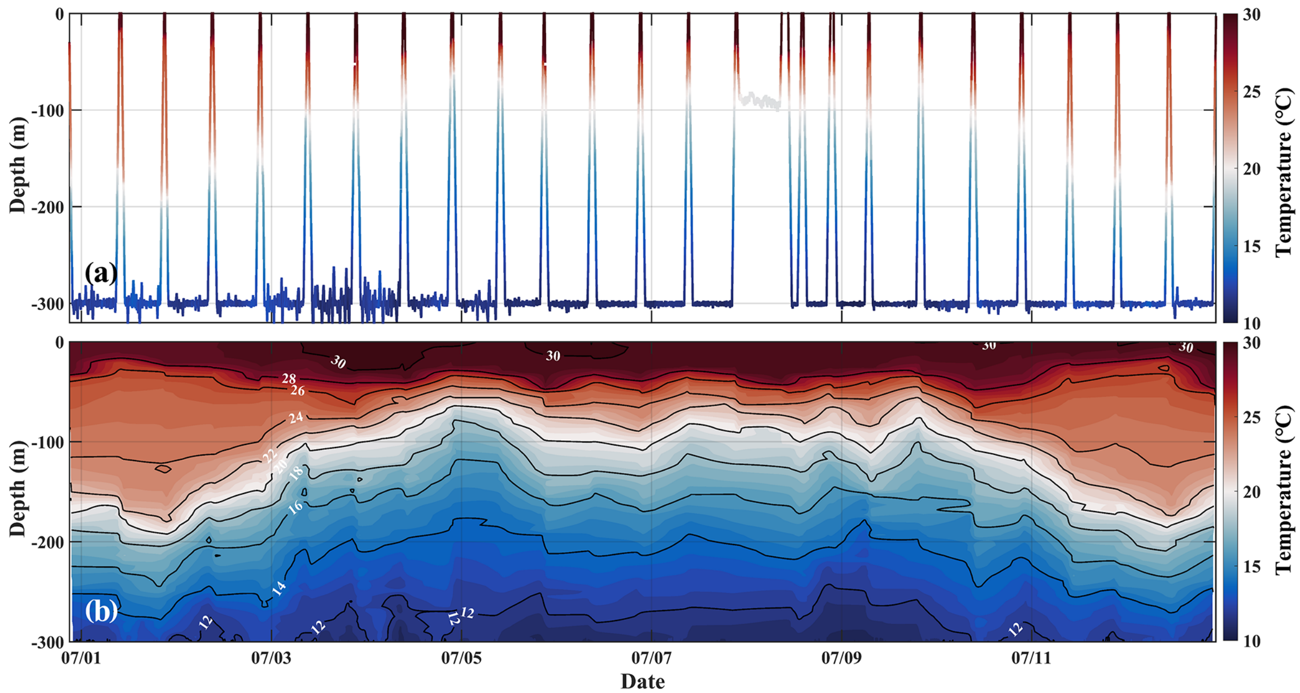

Figure 3. Illustration of **(a)** original and **(b)** interpolated temperature data after quality control. The AUV observation period is July 2021. AUV: autonomous underwater vehicle.

3.1 UG data quality control

Two Chinese UGs named "Sea-Wing" and "Petrel" were employed in this study. These platforms integrate communication and navigation subsystems comprising iridium satellite communication devices, wireless communication devices, a precision navigation attitude sensor, a Global Positioning System (GPS) device, a pressure sensor, an obstacle avoidance sonar, and a CTD sensor with a 6 s sampling interval.

Before investigating oceanic phenomena, we performed data quality control following the integrated ocean observing system (IOOS) standard. The QC procedure for UGs (https://repository.oceanbestpractices.org/handle/11329/289?show=full last access: 17 October 2024) includes nine steps: (1) Timing/gap test: this test determines that the profile has been received within the expected time window and has the correct time stamp. (2) Syntax test: this test ensures the structural integrity of data messages. (3) Location test: this tests if the reported physical location (latitude and longitude) is within the reasonable range determined by the operator. (4) Gross range test: this test ensures that the data points do not exceed the minimum/maximum output range of the sensor. (5) Pressure test: this tests if the pressure records increase monotonically with depth, sorts the vertical depth values, and removes any duplicate depth values. The data obtained after steps (1)–(5) are directly output by the UGs. (6) Climatology test: this tests if the data points are within the seasonal expectation range. (7) Spike test: this tests if the data points exceed the selected threshold compared to adjacent data points, excluding the data with temperature–salinity larger than 35°/35 psu. (8) Rate of change test: this tests if the rate of change in the time series exceeds the threshold determined by the operator. (9) Flat line test: this is a test for continuously repeated observations of the same value, which may be the result of sensor or data collection platform failure. Post-stage (6) and (7) data are designated as *_RO (remove outliers), while the outputs of stages (8) and (9) generate *_TSD (triple standard deviation) following 3σ outlier exclusion.

We performed cross-validation using the UG-observed temperature and salinity profiles and shipborne CTD cast data for July 2019 (Fig. 1e, black star, and Fig. 4). Quantitative analysis revealed that the mean bias of the temperature is 0.05 °C and that of the salinity is 0.01 psu. The vertical temperature–salinity profiles observed by the ship and UG are consistent, supporting the notion that the data are credible.

3.2 AUV data quality control

Both CTD and GPS instruments were installed on the "Sea-Whale 2000" AUV. The platform was designed by the Institute of Shenyang Automation, Chinese Academy of Sciences. It could operate in two modes: "sawtooth" mode and "cruise" mode at a specific depth of 300 m (Huang et al., 2019).

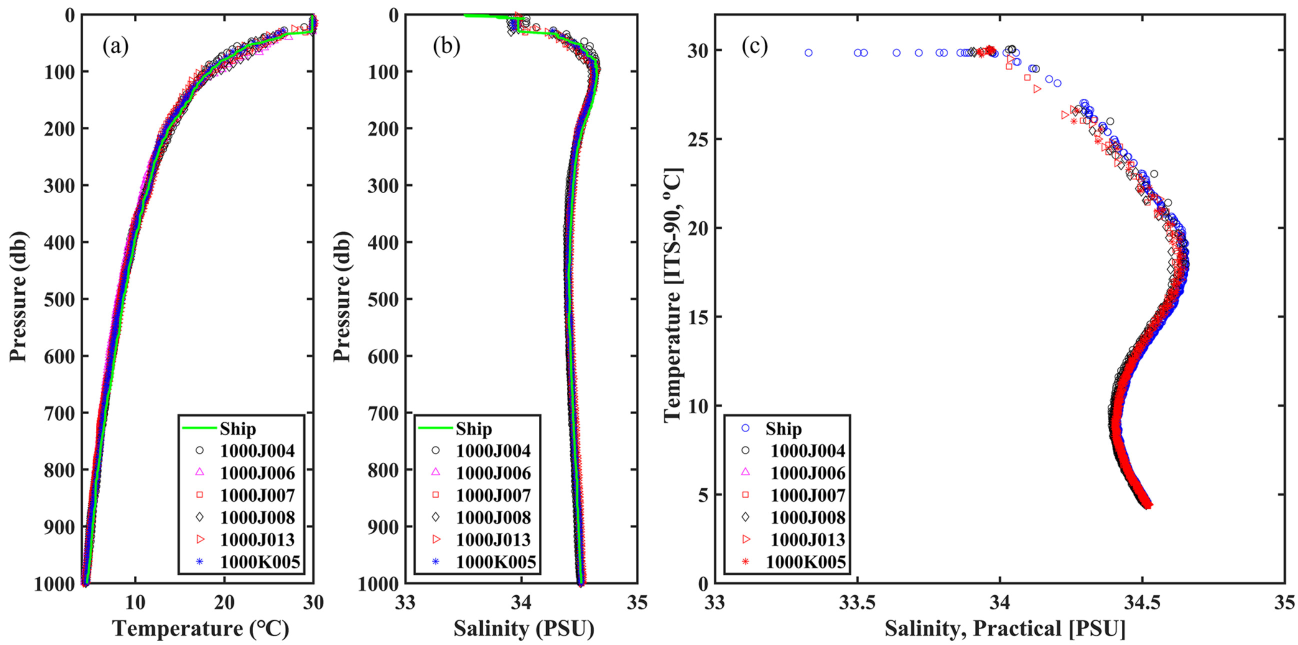

Figure 4. Comparison of **(a)** temperature, **(b)** salinity, and **(c)** temperature–salinity scatter plots between ship-installed CTD and AUV-installed CTD at station (17.7778° N, 112.0661° E). Green line in **(a)** and **(b)** is the ship-measured values. The dot, pink triangle, red square, diamond, red triangle, and blue star correspond to UGs named 1000J004, 1000J006, 1000J007, 1000J008, 1000J013, and 1000K005, respectively.

For the "sawtooth" mode data, we applied identical quality control protocols as described in Sect. 3.1 for UGs (Figs. 3 and 4). In "cruise" mode, the AUV navigates at a depth of around 300 m. Following Qiu et al. (2020), we first transformed the temperature and salinity at depth z to those at 300 m using a linear regression method ($T' = 0.008z' + 0.017$; $S' = -0.0002z' + 0.0006$):

$$T' = T_z - T_{\text{mean}}, \tag{1a}$$

$$S' = S_z - S_{\text{mean}}, \tag{1b}$$

where T_{mean} is averaged using a 10-point smoothed average, which could maintain the spatial variations from 20 to 30 km. The depth anomaly is defined as the measured depth minus 300 m, i.e., $z' = z - 300$, and the temperature and salinity anomalies are defined as T' and S', respectively. Validation against the potential temperature algorithm demonstrated that the temperatures reconstructed at 300 m were highly consistent.

3.3 Density derived from temperature and salinity

Seawater density (ρ, in kg m^{-3}) was computed based on temperature (T, in °C), salinity (S, in psu), and pressure (P, in dbar) using the UNESCO international equation of state (Fofonoff and Millard, 1983). The UNESCO formula provides a simplified approach to estimate seawater density as follows:

$$\rho(S,T,P) = \frac{\rho_0(S,T)}{1 - \frac{P}{K(S,T,P)}}, \tag{2a}$$

$$\rho_0(S,T) = \rho_{\text{sw}}(T) + \left(b_0 + b_1 T_{68} + b_2 T_{68}^2 + b_3 T_{68}^3 + b_4 T_{68}^4\right) S + \left(c_0 + c_1 T_{68} + c_2 T_{68}^2\right) \times S\sqrt{S} + d_0 S^2, \tag{2b}$$

$$\rho_{\text{sw}}(T) = a_0 + a_1 T_{68} + a_2 T_{68}^2 + a_3 T_{68}^3 + a_4 T_{68}^4 + a_5 T_{68}^5, \tag{2c}$$

$$T_{68} = T \times 1.00024, \tag{2d}$$

where $K(S,T,P)$ is the secant bulk modulus and a_0 and others are coefficients. The coefficients follow the original formulation, accounting for nonlinear compressibility effects.

4 Data application

4.1 Subsurface MEs observed by UGs and AUVs

Glider arrays successfully captured the full-depth thermohaline signatures of both warm and cold eddies through cross-eddy transects (Fig. 4). In April 2015, one UG deployment crossed a warm eddy and observed a subsurface warm core (Figs. 1b and 5a), corresponding to the subsurface eddy (50–500 m depth, 100 km radius) as described by Shu et al. (2016). Qiu et al. (2019b) utilized this dataset to investigate the asymmetry structures of this subsurface eddy, suggesting that the centrifugal force should be taken into account

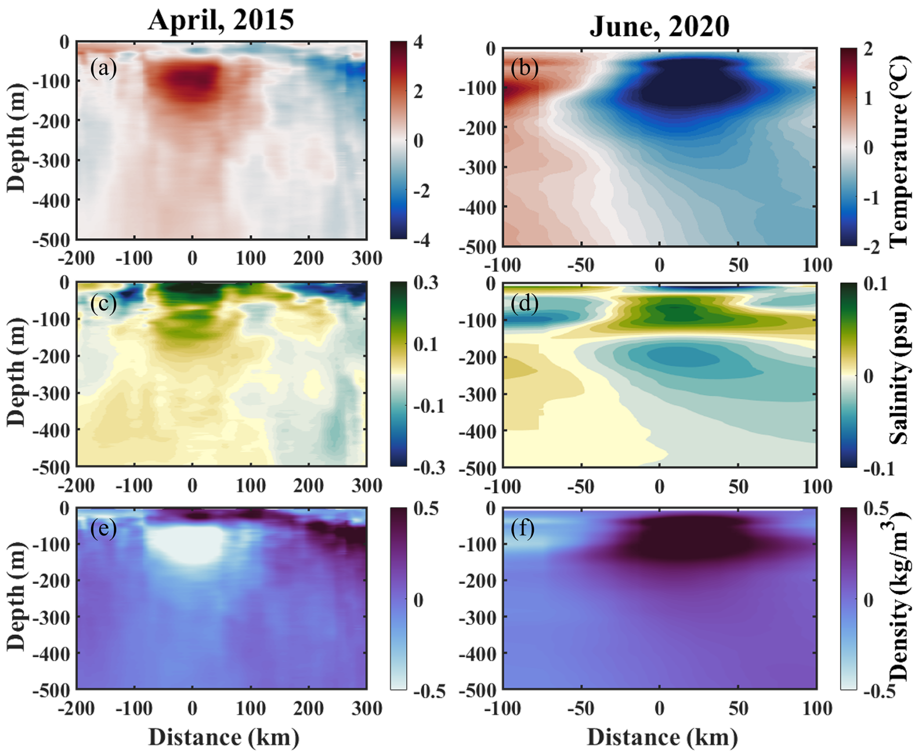

Figure 5. Contours of the **(a)** and **(b)** temperature anomaly, **(c)** and **(d)** salinity anomaly, and **(e)** and **(f)** density anomaly in April 2015 (**a**, **c**, and **e**) and June 2020 (**b**, **d**, and **f**). The contours were generated by interpolating the original data points.

when revealing the velocity of MEs, i.e., gradient wind balance theory. June 2020 glider observations captured a subsurface cold eddy exhibiting pronounced thermohaline anomalies within the main pycnocline layer (Figs. 1g and 5d–f). This density-compensated structure, defined as local deviations from zonal mean conditions, manifested through compensating for temperature and salinity anomalies that generated a baroclinic density core penetrating the upper 500 m. The colocated thermohaline signatures demonstrate the UG's capability to resolve three-dimensional eddy characterization, including core localization, spatial footprint delineation, and dynamic intensity assessment.

Both UGs and AUVs demonstrate the ability to monitor the temporal evolutions of subsurface MEs. During their developmental stages, these vortices exhibit morphological instabilities that induce cross-slope transport along continental margins (Wang et al., 2018; Su et al., 2020; Qiu et al., 2022) while simultaneously generating submesoscale processes through frontal instability (Dong and Zhong, 2018; Yang et al., 2019). To capture the eddy evolution process, we executed five successive AUV transects along rectangular trajectories across an anticyclonic ME during May to July 2021 (Fig. 1h), supported by the National Key Research and Development Program.

Figure 6 illustrates a subsurface-intensified anticyclone occupying the 50–200 m depth stratum, exhibiting weakened stratification with a reduced Brunt–Väisälä frequency squared value ($N^2 = \frac{1}{\rho}\frac{\mathrm{d}\rho}{\mathrm{d}z} < 10^{-4}$). The AUV mission was divided into five discrete phases: $T1$ (8–11 June), $T2$ (19–23 June), $T3$ (29 June-4 July), $T4$ (10–15 July), and $T5$ (21–26 July). Delineating the eddy boundaries using isopycnals at 22.5 and 23.5 kg m^{-3}, we quantified temporal variations in the eddy area and thermal properties. A progressive decline in both areal extent and mean temperature occurred between $T1$ and $T3$, followed by subsequent recovery from $T4$ to $T5$, indicating distinct weakening and reintensification phases. This life cycle aligns with Qiao et al.'s (2023) trajectory analysis documenting eastward propagation during $T1$–$T3$ and topographic trapping during $T4$ and $T5$.

4.2 Vertical tilt of MEs at different life stages observed by UGs

Coordinated glider deployments were executed in 2015, 2017, 2019, and 2020 to resolve ME dynamics. The complete ME life cycle progresses through four distinct phases, i.e., birth, development, maturity, and dissipation stages (Zhang and Qiu, 2018; Yang et al., 2019), with each phase exhibiting different kinetic energy budgets. The Luzon Strait serves as an eddy birth zone, where the Kuroshio branch intrudes the SCS (Chen et al., 2011; Su et al., 2020). After birth, most of the eddies move westward to the continental shelf zone under the modulation of a Rossby wave before finally dissipating in

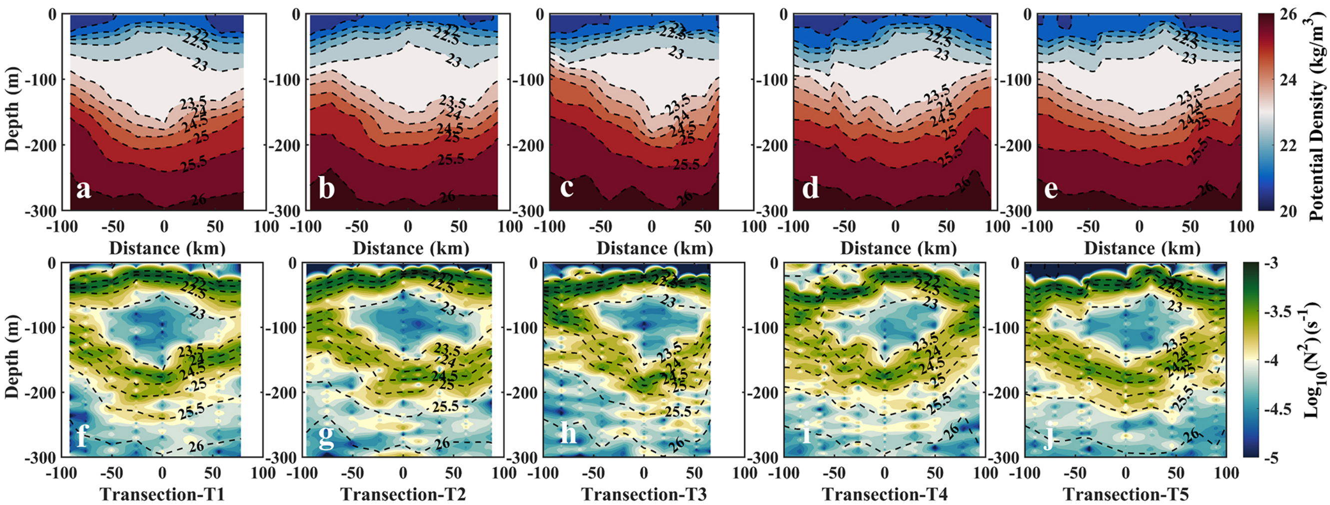

Figure 6. The profiles of density **(a–e)** and Brunt frequency **(f–j)** during **(a, f)** T1, **(b, g)** T2, **(c, h)** T3, **(d, i)** T4, and **(e, j)** T5 in 2021, which correspond to 06/08–06/11, 06/19–06/23, 06/29–07/04, 07/10–07/15, 07/21–07/26, respectively. The contours were generated by interpolating the original data points.

the Dongsha Islands and Xisha Islands or merging with other eddies (Yang et al., 2019; Su et al., 2020; Qiu et al., 2022).

These deployments of AUVs and UGs enabled three-dimensional structural characterization across the ME life stages. Quality-controlled temperature–salinity profiles were interpolated into 1 km × 1 km × 1 m grids prior to density (ρ) computation. Assuming geostrophic balance, the geostrophic velocity, v_g, could be derived under the force balances between the pressure gradient and Coriolis forces:

$$v_g(xyz) = v_0 - \frac{g}{f\rho_0}\int_{z0}^{z}\left(\frac{\partial\rho(x,y,z)}{\partial x} + \frac{\partial\rho(x,y,z)}{\partial y}\right)\mathrm{d}z, \quad (3)$$

where ρ_0 is the referenced water density, f is the Coriolis frequency, and v_0 (set to 0) represents the referenced geostrophic velocity at depth 1000 m.

The July 2019 deployment (12 UGs, 120° E) observed the three-dimensional temperature and geostrophic velocity structures of an ME in the birth stage and captured the subsurface warm core exhibiting a northeastward vertical tilt (solid black line in Fig. 7). The July 2017 observations (10 UGs, 119° E) revealed a developing eddy that exhibited an eastward tilt through a 500 m water column, which may be attributed to combined forcing from westward-propagating Rossby waves and background current shear (e.g., Qiu et al., 2015; Zhang et al., 2016), as well as thermal front advection (e.g., Bonnici and Billant, 2020; Gaube et al., 2015). Throughout this experiment, the UGs encountered the tropical storm "Haitang", resulting in the ME undergoing horizontal deformation and giving rise to submesoscale processes (Yi et al., 2022; Yi et al., 2024).

The June 2020 observations (12 gliders; Figs. 1g and 6e–h) documented a dissipating anticyclone with a southwestward tilt from 500 m to the surface (Fig. 7e and f). This kind of southwestward vertical tilt was revealed in a numerical model, which showed that the steep topography caused asymmetries of the velocities within the MEs (Qiu et al., 2022). The June 2021 AUV measurements (Qiao et al., 2023; Fig. 1h) further captured an eastward movement of the ME, which was dominated by wave-current interactions.

4.3 Submesoscale instabilities at the edge of MEs observed by UGs

Submesoscale processes usually occur within MEs, either at the eddy peripheries (front; filament) or entrained in the eddy center, in terms of spiral structures or "eye-cat" structures (Zhang and Qiu, 2018; Ni et al., 2021; Hu et al., 2023; Qiu et al., 2024a). These processes facilitate bidirectional energy transfers, driving forward cascades to dissipating scales through symmetric and centrifugal instabilities while simultaneously energizing inverse energy pathways to MEs via mixed-layer baroclinic instabilities (i.e., Fox-Kemper et al., 2008; McWilliams, 2016). Conventional Argo floats, constrained by 10 d sampling intervals, provide insufficient data to resolve rather short-duration features. Recent technological advancement reveals diverse observational capabilities. For example, Lagrangian platforms, like NAVIS floats, have identified frontal genesis dominated by mixed-layer baroclinic instability (Tang et al., 2022), while glider arrays employing virtual mooring configurations achieve Eulerian frontal characterization through programmable sampling strategies (Qiu et al., 2019a; Shang et al., 2023). This methodological contrast highlights glider advantages in enabling simultaneous cross-front and along-front measurements through active navigation, overcoming the spatial limitations inherent to passive Lagrangian drifters.

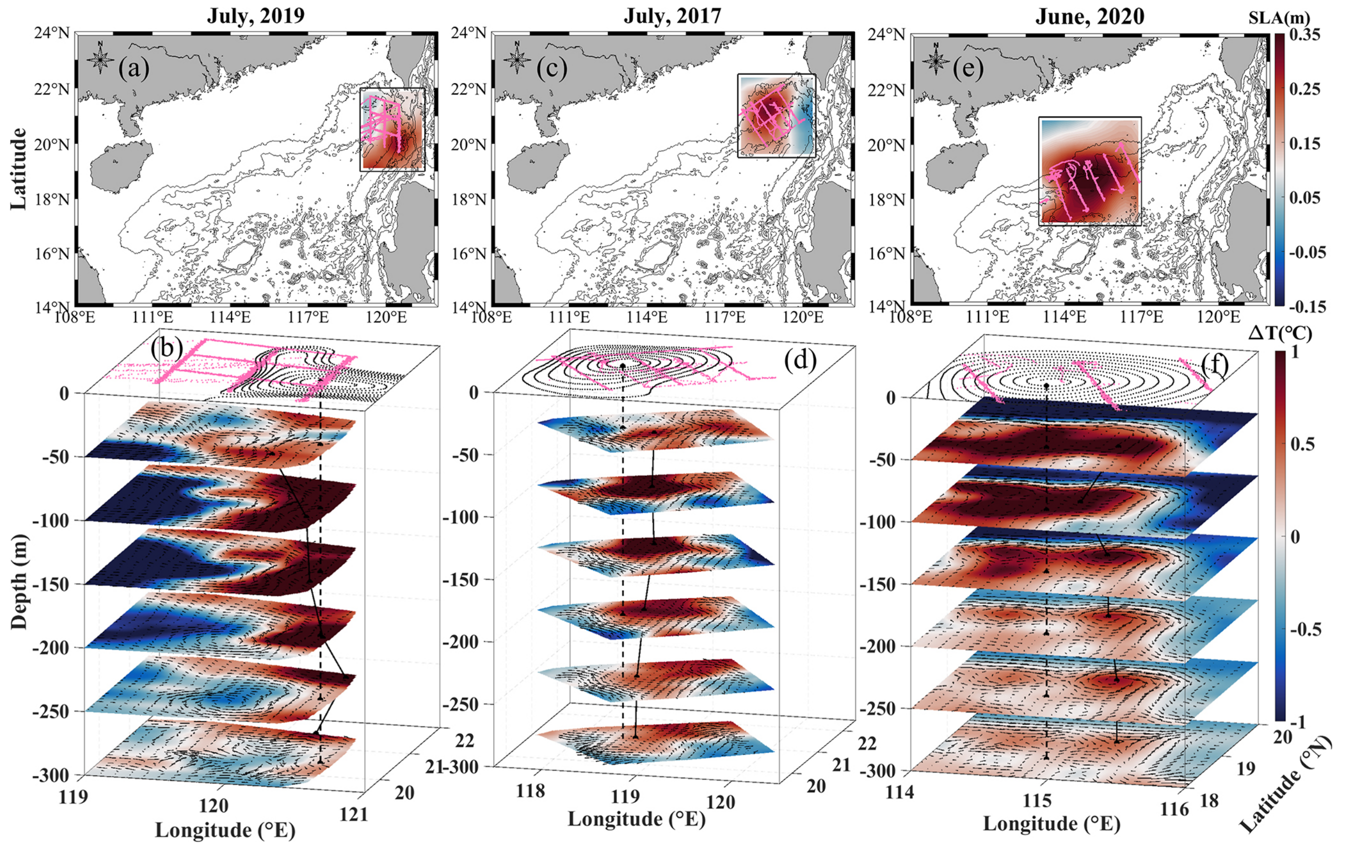

Figure 7. Eddy structures during periods of **(a, b)** eddy birth, **(c, d)** westward movement, and **(e, f)** dissipation along the slope. Sea level anomaly (SLA) and UG positions are superimposed in the upper panels (**a**, **c**, and **e**); isobaths are represented by solid lines. The UG-observed temperature and derived geostrophic velocities are shown in the 3D plots (**b**, **d**, and **f**). Pink lines are the tracks of UGs. Dashed lines denote the centers of mesoscale eddies from SLA fields, and solid lines show the centers of the warm cores at each depth. UG: underwater glider. The contours were generated by interpolating the original data points.

Our observational dataset reveals that 40 % of UG missions resolved submesoscale processes (< 3 km horizontal resolution, < 4 h temporal resolution; Fig. 2). To demonstrate this operational advantage, we analyzed two representative cases of submesoscale instabilities along ME peripheries.

The 2017 deployment illustrates multi-platform sampling strategies, with four UGs strategically positioned at an anticyclonic ME boundary (Fig. 8a). Three UGs executed cross-front transects, while one maintained along-front tracking, enabling comprehensive instability characterization through the Richardson number phase angle, ϕ_{Ri}, defined as,

$$\phi_{Ri} = \tan^{-1}\left(-\frac{1}{Ri}\right) = \tan^{-1}\left(\frac{|\nabla \cdot b|^2}{N^2 \cdot f^2}\right), \tag{4a}$$

$$Ri \approx Ri_{\mathrm{g}} = \frac{N^2}{\left(\frac{\partial \boldsymbol{v}_{\mathrm{g}}}{\partial z}\right)^2} = \frac{N^2 \cdot f^2}{|\nabla \cdot b|^2} < \frac{f}{\zeta_{\mathrm{g}}} \text{ and } f \cdot \zeta_{\mathrm{g}} > 0, \tag{4b}$$

where $b = -g\rho/\rho_0$ is the buoyancy flux and g is the gravitational acceleration. $N^2 = \partial b/\partial z$ is the vertical buoyancy frequency. $\zeta_{\mathrm{g}} = \mathrm{curl}(\boldsymbol{v}_{\mathrm{g}})$ is the vertical relative vorticity (Thomas et al., 2013). For anticyclonic eddies, inertial instability or symmetric instability occurs when $-45° < \phi_{Ri} < \phi_c$. $\phi_c = \tan^{-1}(-(f+\zeta_{\mathrm{g}})/f)$ is the critical angle. Only symmetric instability occurs when $-90° < \phi_{Ri} < -45°$; symmetric instability or gravitational instability occurs when $-135° < \phi_{Ri} < -90°$; and gravitational instability occurs when $-180° < \phi_{Ri} < -135°$.

The 2017 dataset revealed coexisting gravitational, symmetric, and centrifugal-symmetric instabilities along the ME periphery (Fig. 8a). Figure 8b shows submesoscale instabilities in 2019. In this case, gravity instability dominates the upper mixed layer, while symmetric and centrifugal instabilities are not significant. These two cases provide us enough information to detect frontal genesis processes in Eulerian view, while NAVIS or Argo devices provide frontal information in Lagrangian view.

5 Data availability

The dataset of temperature–salinity observed by AUVs and UGs in this paper was deposited in the Science Data Bank,

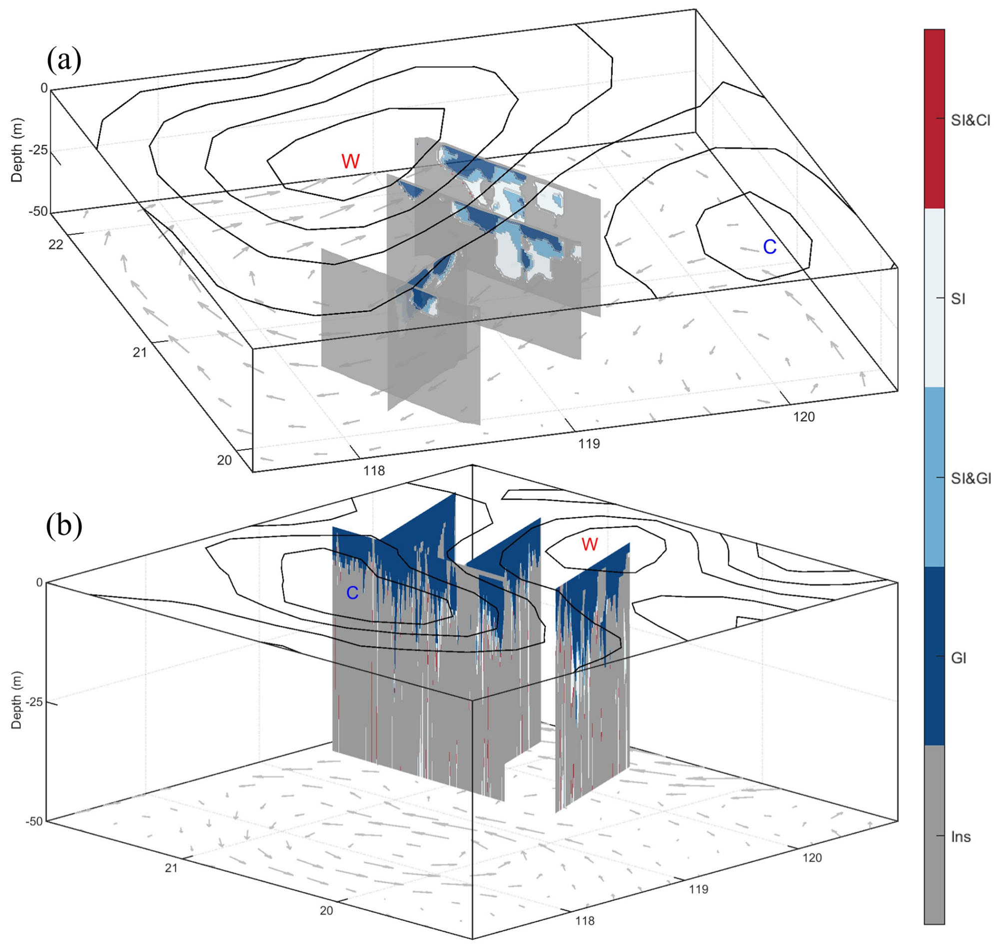

Figure 8. Analyzed submesoscale instabilities at the edge of mesoscale eddies in **(a)** 2017 and **(b)** 2019. SI: symmetric instability; CI: centrifugal instability; GI: gravity instability; W: anticyclonic eddy; C: cyclonic eddy. Isolines are the sea level anomalies, and vectors are the geostrophic velocities. The contours were generated by interpolating the original data points.

whose DOI is https://doi.org/10.57760/sciencedb.11996 (Qiu et al., 2024b). The dataset includes two files: "Grid_data" and "Observation_data".

6 Conclusions and potential future plan

Our 9-year AUV and UG observations yielded a dataset of high-resolution temperature and salinity profiles for the SCS. This comprehensive compilation comprises 13 491 profiles and covers 463 d' experiments, encompassing 11 experiments deploying 50 UGs and two AUVs. To our knowledge, this represents the first multi-platform dataset with sufficient spatio-temporal coverage in detecting the horizontal asymmetry, vertical tilt, temporal evolution, and life cycle of MEs (Fig. 9) while simultaneously capturing associated submesoscale processes. The dataset allows us to investigate the subsurface MEs, revealing eddy-current and eddy-topography interactions successfully. However, to quantify ME feedbacks based on the variability of larger-scale currents, i.e., western boundary current, long-term routine UG and AUV observations are needed in the future.

Beyond tracking MEs, UGs and AUVs have been proved to actively capture smaller-scale oceanic processes. Successful applications include internal tide (Gao et al., 2024) and turbulent dissipation rates by using turbulent parameterization schemes (Qi et al., 2020). Moreover, UGs/AUVs equipped with more sensors could provide us geochemical parameters (e.g., Yi et al., 2022), potentially enhancing coupled physical-biogeochemical model forecasting through data assimilation. More projects gathering an AUV network are ongoing and will be promoted in the future.

Operational challenges encountered during the program include the following: (1) under a strong background current, UGs and AUVs get disturbed and cannot follow the customized routes; (2) during extreme meteorological conditions, it is difficult for the piloting team to deploy and recover UGs and AUVs; and (3) data-receiving capacity depends on the satellite transmission capacity. If both the biochemistry and CTD data are included, the data resolution

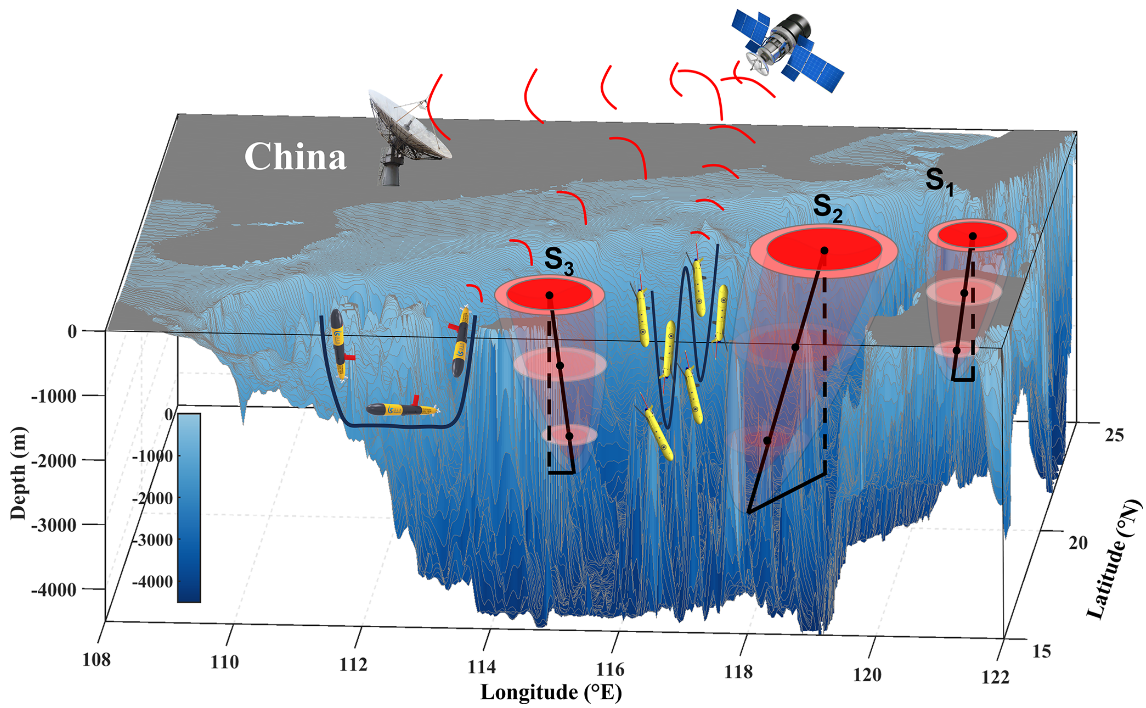

Figure 9. Schematic of UG operations conducted to observe mesoscale eddies at different life stages. S1: birth stage; S2: development/maturity stage; S3: dissipation stage.

has to be lowered. Addressing these challenges requires synergistic collaboration between field operations teams, platform engineers, and dynamical oceanographers to optimize autonomous sampling systems.

Author contributions. Conceptualization: DX; data curation: CH, ZY, ZH, JW; formal analysis: CH, ZY; funding acquisition: CH, DX; investigation: CH, DX; methodology: CH, DX; project administration: CH, DX; software: CH, HB, DX; supervision: CH, DX; validation: XM, DX, WB; writing: CH, XM, HB. All the authors have read and agreed to the published version of the paper.

Competing interests. The contact author has declared that none of the authors has any competing interests.

Disclaimer. Publisher's note: Copernicus Publications remains neutral with regard to jurisdictional claims made in the text, published maps, institutional affiliations, or any other geographical representation in this paper. While Copernicus Publications makes every effort to include appropriate place names, the final responsibility lies with the authors.

Acknowledgements. We acknowledge all the colleagues and project members who have contributed to the design of UGs and AUVs, the sea experiments, and data processing in the past. Many scientists, engineers, and students have participated in active surveys and mappings.

Financial support. This research has been supported by the National Natural Science Foundation of China (grant nos. 42376011 and 42227901) and the National Key Research and Development Program of China (grant no. 2017YFC0305804).

Review statement. This paper was edited by Sebastiano Piccolroaz and reviewed by four anonymous referees.

References

Bonnici, J. and Billant, P.: Evolution of a vortex in a strongly stratified shear flow. Part 1. Asymptotic analysis, J. Fluid Mech., 893, A17, https://doi.org/10.1017/jfm.2020.226, 2020.

Caffaz, A., Caiti, A., Casalino, G., and Turetta, A.: The hybrid glider/AUV folaga, IEEE Robot. Autom. Mag., 17, 31–44, https://doi.org/10.1109/MRA.2010.935791, 2010.

Chelton, D., Schlax, M., Samelson, R., and de Szoeke, R.: Global observations of large oceanic eddies, Geophys. Res. Lett., 34, L15606, https://doi.org/10.1029/2007GL030812, 2007.

Chelton, D., Schlax, M., and Samelson, R.: Global observations of nonlinear mesoscale eddies, Prog. Oceanogr., 91, 167–216, https://doi.org/10.1016/j.pocean.2011.01.002, 2011.

Chen, G., Hou, Y., and Chu, X.: Mesoscale eddies in the South China Sea: Mean properties, spatiotemporal variability, and impact on thermohaline structure, J. Geophys. Res.-Oceans, 116, C06018, https://doi.org/10.1029/2010JC006716, 2011.

Chu, P., Chen, Y., and Lu, S.: Wind-driven South China Sea deep basin warm-core/cool-core eddies, J. Oceanogr., 54, 347–360, https://doi.org/10.1007/bf02742619, 1998.

Dale, W.: Winds and drift currents in the South China Sea, Malayan Journal of Tropical Geography, 8, 1–31, 1956.

Dong, J. and Zhong, Y.: The spatiotemporal features of submesoscale processes in the northeastern South China Sea, Acta Oceanol. Sin., 37, 8–18, https://doi.org/10.1007/s13131-018-1277-2, 2018.

Fang, W., Fang, G., Shi, P., Huang, Q., and Xie, Q.: Seasonal structures of upper layer circulation in the southern South China Sea from in situ observations, J. Geophys. Res.-Oceans, 107, 23–1-23-2, https://doi.org/10.1029/2002JC001343, 2002.

Fofonoff, N. P. and Millard, R. C.: Algorithms for computation of fundamental properties of seawater, UNESCO Tech. Pap. in Mar. Sci., Spectrochim. Acta Pt. A, 44, 53, https://doi.org/10.1016/j.saa.2012.12.093, 1983.

Fox-Kemper, B., Ferrari, R., and Hallberg, R.: Parameterization of mixed layer eddies. Part I: Theory and diagnosis, J. Phys. Oceanogr., 38, 1145–1165, https://doi.org/10.1175/2007JPO3792.1, 2008.

Gao, Z., Chen, Z., Huang, X., Yang, H., Wang, Y., Ma, W., and Luo, C.: Estimating the energy flux of internal tides in the northern South China Sea using underwater gliders, J. Geophys. Res.-Oceans, 129, e2023JC020385, https://doi.org/10.1029/2023JC020385, 2024.

Gaube, P., Chelton, D. B., Samelson, R. M., Schlax, M. G., and O'Neill, L. W.: Satellite Observations of Mesoscale Eddy-Induced Ekman Pumping, J. Phys. Oceanogr., 45, 104–132, https://doi.org/10.1175/JPO-D-14-0032.1, 2015.

He, Q., Zhan, H., Cai, S., He, Y., Huang, G., and Zhan, W.: A new assessment of mesoscale eddies in the South China Sea: surface features, three-dimensional structures, and thermohaline transports, J. Geophys. Res.-Oceans, 123, 4906–4929, https://doi.org/10.1029/2018JC014054, 2018.

He, Q., Zhan, H., Xu, J., Cai, S., Zhan, W., Zhou, L., and Zha, G.: Eddy-induced chlorophyll anomalies in the western South China Sea, J. Geophys. Res.-Oceans, 124, https://doi.org/10.1029/2019JC015371, 2019.

He, Y., Xie, J., and Cai, S.: Interannual variability of winter eddy patterns in the eastern South China Sea, Geophys. Res. Lett., 43, 5185–5193, https://doi.org/10.1002/2016GL068842, 2016.

Hobson, B. W., Bellingham, J. G., Kieft, B., McEwen, R., Godin, M., and Zhang, Y.: Tethys-class long range AUVs - extending the endurance of propeller-driven cruising AUVs from days to weeks, in: IEEE/OES Autonomous Underwater Vehicles (AUV), Southampton, UK, 24–27 September 2012, 1–8, https://doi.org/10.1109/AUV.2012.6380735, 2012.

Hu, Z., Lin, H., Liu Z., Cao Z., Zhang F., Jiang Z., Zhang Y., Zhou K., and Dai M.: Observations of a filamentous intrusion and vigorous submesoscale turbulence within a cyclonic mesoscale eddy, J. Phys. Oceanogr., 53, 1615–1627, https://doi.org/10.1175/JPO-D-22-0189.1, 2023.

Huang, Y., Qiao, J., Yu, J., Wang, Z., Xie, Z., and Liu, K.: Sea-Whale 2000: a long-range hybrid autonomous underwater vehicle for ocean observations, in: OCEANS 2019 – Marseille, Marseille, France, 17–20 June 2019, 1–6, https://doi.org/10.1109/OCEANSE.2019.8867050, 2019.

Hwang, C. and Chen, S.: Circulations and eddies over the South China Sea derived from TOPEX/Poseidon altimetry, J. Geophys. Res.-Oceans, 105, 23943–23965, https://doi.org/10.1029/2000JC900092, 2000.

Li, H., Xu, F., and Wang, G.: Global mapping of mesoscale eddy vertical tilt, J. Geophys. Res.-Oceans, 127, e2022JC019131, https://doi.org/10.1029/2022JC019131, 2022.

Li, L., Worth, D., Nowlin, J., and Su. J.: Anticyclonic rings from the Kuroshio in the South China Sea, Deep-Sea Res. Pt. I, 45, 1469–1482, https://doi.org/10.1016/s0967-0637(98)00026-0, 1998.

Lin, P., Wang, F., Chen, Y., and Tang, X.: Temporal and spatial variation characteristics of eddies in the South China Sea I: Statistical analyses, Acta Oceanol. Sin., 29, 14–22, https://doi.org/10.3321/j.issn:0253-4193.2007.03.002, 2007.

McWilliams, J.: Submesoscale currents in the ocean, P. R. Soc. A-Math. Phy., 472, 20160117, https://doi.org/10.1098/rspa.2016.0117, 2016.

Morrow, R., Birol, F., Griffin, D., and Sudre, J.: Divergent pathways of cyclonic and anti-cyclonic ocean eddies, Geophys. Res. Lett., 31, L24311, https://doi.org/10.1029/2004gl020974, 2004.

Nan, F., He, Z., Zhou, H., and Wang, D.: Three long-lived anticyclonic eddies in the northern South China Sea, J. Geophys. Res.-Oceans, 116, C05002, https://doi.org/10.1029/2010JC006790, 2011.

Ni, Q., Zhai, X., Wilson, C., Chen, C., and Chen, D.: Submesoscale eddies in the South China Sea, Geophys. Res. Lett., 48, e2020GL091555, https://doi.org/10.1029/2020GL091555, 2021.

Oey, L.: Eddy- and wind-forced shelf circulation, J. Geophys. Res., 100, 8621–8637, https://doi.org/10.1029/95JC00785, 1995.

Okkonen, S., Weingartener, T., Danielson, S., Musgrave, D., and Schmidt, G. M.: Satellite and hydrographic observations of eddy-induced shelf-slope exchange in the northwestern Gulf of Alaska, J. Geophys. Res., 108, 3033, https://doi.org/10.1029/2002JC001342, 2003.

Qi, Y., Shang, C., Mao, H., Qiu, C., and Shang, X.: Spatial structure of turbulent mixing of an anticyclonic mesoscale eddy in the northern South China Sea, Acta Oceanol. Sin., 39, 69–81, https://doi.org/10.1007/s13131-020-1676-z, 2020.

Qiao, J., Qiu, C., Wang, D., Huang, Y., Zhang, X., and Huang, Y.: Multi-stage Development within Anisotropy Insight of an Anticyclone Eddy Northwestern South China Sea in 2021, Geophys. Res. Lett., 50, 19, https://doi.org/10.1029/2023GL104736, 2023.

Qiu, C., Mao, H., Yu, J., Xie, Q., Wu, J., Lian, S., and Liu, Q.: Sea surface cooling in the Northern South China Sea observed using Chinese Sea-wing Underwater Glider Measurements, Deep-Sea Res. Pt. I, 105, 111–118, https://doi.org/10.1016/j.dsr.2015.08.009, 2015.

Qiu, C., Mao, H., Liu, H., Xie, Q., Yu, J., Su, D., Ouyang, J., and Lian, S.: Deformation of a warm eddy in the northern South China Sea, J. Geophys. Res.-Oceans, 124, 5551–5564, https://doi.org/10.1029/2019JC015288, 2019a.

Qiu, C., Mao, H., Wang, Y., Su, D., and Lian, S.: An irregularly shaped warm eddy observed by Chinese underwater gliders, J. Oceanogr., 75, 139–148, https://doi.org/10.1007/s10872-018-0490-0, 2019b.

Qiu, C., Liang, H., Huang, Y., Mao, H., Yu, J., Wang, D., and Su, D.: Development of double cyclonic mesoscale eddies at around Xisha Islands observed by a 'Sea-Whale 2000' autonomous underwater vehicle, Appl. Ocean Res., 101, 102270, https://doi.org/10.1016/j.apor.2020.102270, 2020.

Qiu, C., Yi, Z., Su, D., Wu, Z., Liu, H., Lin, P., He, Y., and Wang, D.: Cross-slope heat and salt transport induced by slope intrusion eddy's horizontal asymmetry in the northern South China Sea, J. Geophys. Res.-Oceans, 127, e2022JC018406, https://doi.org/10.1029/2022JC018406, 2022.

Qiu, C., Yang, Z., Feng, M., Yang, J., Rippeth, T. P., Shang, X., Sun, Z., Jing, C., and Wang, D.: Observational energy transfers of a spiral cold filament within an anticyclonic eddy, Prog. Oceanogr., 220, 1.1–1.12, https://doi.org/10.1016/j.pocean.2023.103187, 2024a.

Qiu, C., Du, Z., Tang, H., Yi, Z., Qiao, J., Wang, D., Zhai, X., and Wang, W.: A High-Resolution Temperature-Salinity Dataset Observed by Autonomous Underwater Vehicles for the Evolution of Mesoscale Eddies and Associated Submesoscale Processes in South China Sea, Science Data Bank [data set], https://doi.org/10.57760/sciencedb.11996, 2024b.

Rainville, L., Lee, C., Arulananthan, K., Jinadasa, S., Fernando, H., Priyadarshani, W., and Wijesekera, H.: Water mass exchanges between the Bay of Bengal and Arabian Sea from multiyear sampling with autonomous gliders, J. Phys. Oceanogr., 52, 2377–2396, https://doi.org/10.1175/JPO-D-21-0279.1, 2022.

Rudnick, D. L., Davis, R. E., Eriksen, C. C., Fratantoni, D. M., and Perry, M. J.: Underwater Gliders for Ocean Research, Mar. Technol. Soc. J., 38, 73–84, https://doi.org/10.4031/002533204787522703, 2004.

Shang, X., Shu, Y., Wang, D., Yu, J., Mao, H., Liu, D., Qiu, C., and Tang, H.: Submesoscale motions driven by down-front wind around an anticyclonic eddy with a cold core, J. Geophys. Res.-Oceans, 128, e2022JC019173, https://doi.org/10.1029/2022JC019173, 2023.

Shu, Y., Xiu, P., Xue, H., Yao, J., and Yu, J.: Glider-observed anticyclonic eddy in northern South China Sea, Aquat. Ecosyst. Health, 19, 233–241, https://doi.org/10.1080/14634988.2016.1208028, 2016.

Su, D., Lin, P., Mao, H., Wu, J., Liu, H., Cui, Y., and Qiu, C.: Features of slope intrusion mesoscale eddies in the northern South China Sea, J. Geophys. Res.-Oceans, 125, e2019JC015349, https://doi.org/10.1029/2019JC015349, 2020.

Tang, H., Shu, Y., Wang, D., Xie, Q., Zhang, Z., Li, J., Shang, X., Zhang, O., and Liu, D.: Submesoscale processes observed by high-frequency float in the western South China Sea, Deep-Sea Res. Pt. I, 192, 103896, https://doi.org/10.1016/j.dsr.2022.103896, 2022.

Thomas, L., Taylor, J., Ferrari, R., and Terrence M.: Symmetric instability in the Gulf Stream, Deep-Sea Res. Pt. II, 91, 96–110, https://doi.org/10.1016/j.dsr2.2013.02.025, 2013.

Todd, R. E. and Ren, A. S.: Warming and lateral shift of the Gulf Stream from in situ observations since 2001, Nat. Clim. Change, 13, 1348–1352, https://doi.org/10.1038/s41558-023-01835-w, 2023.

Wang, G., Su, J., and Chu, P.: Mesoscale eddies in the South China Sea observed with altimetry, Geophys. Res. Lett., 30, 2121, https://doi.org/10.1029/2003GL018532, 2003.

Wang, J.: The warm-core eddy in the northern South China Sea, I. Preliminary observations on the warm-core eddy, Acta Oceanogr. Taiwanica, 18, 92–103, 1987.

Wang, Q., Zeng, L., Li, J., Chen, J., He, Y., Yao, J., Wang, D., and Zhou, W.: Observed Cross-Shelf Flow Induced by Mesoscale Eddies in the Northern South China Sea, J. Phys. Oceanogr., 48, 1609–1628, https://doi.org/10.1175/JPO-D-17-0180.1, 2018.

Wu, J., Zhang, M., and Sun, X.: Hydrodynamic characteristics of the main parts of a hybrid-driven underwater glider PETREL, in: Autonomous Underwater Vehicles, edited by: Nuno A. Cruz, The Institution of Engineering and Technology, London, UK, https://doi.org/10.5772/24750, 2011.

Xiu, P., Chai, F., Shi, L., Xue, H., and Chao, Y.: A census of eddy activities in the South China Sea during 1993-2007, J. Geophys. Res.-Oceans, 115, C03012, https://doi.org/10.1029/2009JC005657, 2010.

Xu, J. and Su, J.: Hydrographic analysis of Kuroshio intrusion into the South China Sea II: Observations during August to September 1994, Tropical Oceanography, 2, 1–23, 1997.

Yang, Q., Nikurashin, M., Sasaki, H., Sun, H., and Tian, J.: Dissipation of mesoscale eddies and its contribution to mixing in the northern South China Sea, Sci. Rep.-UK, 9, 556, https://doi.org/10.1038/s41598-018-36610-x, 2019.

Yi, Z., Wang, D., Qiu, C., Mao, H., Yu, J., and Lian, S.: Variations in dissolved oxygen induced by a tropical storm within an anticyclone in the Northern South China Sea, J. Ocean U. China, 21, 1084–1098, https://doi.org/10.1007/s11802-022-4992-4, 2022.

Yi, Z., Qiu, C., Wang, D., Cai, Z., Yu, J., and Shi, J.: Submesoscale kinetic energy induced by vertical buoyancy fluxes during the tropical cyclone Haitang, J. Geophys. Res.-Oceans, 129, e2023JC020494, https://doi.org/10.1029/2023JC020494, 2024.

Yu, J., Zhang, A, Jing, W. Chen, Q. Tian, Y., and Liu, W.: Development and Experiments of the Sea-Wing Underwater Glider, China Ocean Eng., 25, 721–736, https://doi.org/10.1007/s13344-011-0058-x, 2011.

Zhang, Z. and Qiu, B.: Evolution of submesoscale ageostrophic motions through the life cycle of oceanic mesoscale eddies, Geophys. Res. Lett., 45, 11847–11855, https://doi.org/10.1029/2018GL080399, 2018.

Zhang, Z., Tian, J., Qiu, B., Zhao, W., Chang, P., and Wu, D.: Observed 3D Structure, Generation, and Dissipation of Oceanic Mesoscale Eddies in the South China Sea, Sci. Rep.-UK, 6, 24349, https://doi.org/10.1038/srep24349, 2016.

Zhang, Z., Zhao, W., Qiu, B., and Tian, J.: Anticyclonic eddy sheddings from Kuroshio loop and the accompanying cyclonic eddy in the Northeastern South China Sea, J. Phys. Oceanogr., 47, 1243–1259, https://doi.org/10.1175/JPO-D-16-0185.1, 2017.